

The effects of Ca addition on corrosion and discharge performance of commercial pure aluminum alloy 1070 as anode for Aluminum-air battery

Ting Xu, Zhengfei Hu*, Cheng Yao

Shanghai Key Laboratory for R&D and Application of Metallic Functional Materials, School of Materials Science and Engineering, Tongji University, No. 4800 Cao'an Road, Shanghai 201804, China

*E-mail: huzhengf@tongji.edu.cn

Received: 16 October 2018 / Accepted: 11 December 2018 / Published: 7 February 2019

The effects of calcium addition on the commercial pure aluminum alloy anode for Al-air battery in alkaline electrolyte were examined by potentiodynamic polarization, AC impedance, corrosion rate and discharge measurements. The results show that calcium addition can increase the polarization resistance, discharge voltage and restrain the corrosion rate in 4 M KOH. Electrodes with calcium addition have the superior anode efficiency and higher capacity density. Microstructure observations show that calcium addition refines the grain structure, redistributes the impurity elements Fe and Si, and leads to more intermetallic phases formed along the inter-dendritic region and grain boundary and dispersed in the matrix. These characteristics are responsible for the improved electrochemical performance of the Al-air battery.

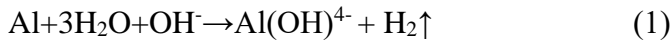
Keywords: Commercial pure aluminum; Ca addition; Microstructure; Corrosion; Discharge behavior

1. INTRODUCTION

The aluminum-air battery as an environmentally friendly and high-theoretical-energy-density system has attracted considerable attention in research and development since the 1960s [1,2]. As reported [3-8], the theoretical cell voltage and energy density of aluminum-air battery are 2.7 V and 8076 Wh kg⁻¹, respectively. In addition, the practical specific energy of 400 Wh kg⁻¹ in this system is also superior to other metal-air batteries. The commercial aluminum alloys for aluminum-air battery are an attractive technology due to their unique combination of being nontoxic and inexpensive and having easy processing [6] compared with other energy technologies.

It is well known that the surface of aluminum alloys can quickly form a protective oxide film when in contact with the air or electrolyte [1]. As a result of this film, the aluminum anode exhibits

polarization, and its corrosion potential moves towards the positive direction under the current load. In addition, the major problem is the low coulombic efficiency in aluminum-air battery. Within the alkaline electrolyte, the aluminum-air battery is accompanied by an undesired hydrogen evolution reaction in the reaction equation (1) during the discharge process [4,6,9]. This high rate of parasitic corrosion results in aluminum mass and conductivity losses [10]. Both serious polarization and corrosion limit commercial applications of aluminum-air batteries.



To avoid these problems, researchers have focused on reducing polarization and accelerating the rate of oxidation while slowing down the hydrogen evolution reaction. One typical way is a small amount of alloying elements to pure aluminum to increase the activation of the anodes, such as Mg, Ga, Hg and Sn, or to decrease the corrosion rate such as with Pb, In, Zn, and Sn [4,11-17]. Another method is to change the microstructure of the anode, which is related to the electrochemical and discharge behavior [10]. The composition and structure of anode have a great influence on the properties of the battery.

Some commercial aluminum alloys used as anodes for Al-air alkaline batteries, such as 1085, 2024, 6013 and 7075, have been investigated [6,18,19]. The composition and structure of the anodes have a great influence on the properties of the battery. These research works indicate that the commercial aluminum alloys provided various electrochemical performances for their complex compositions, and sometimes they have positive effects on battery efficiency and decrease the corrosion rate. Due to the anode of pure aluminum or trace alloyed showing much better battery efficiency [4,20], it is expected that the commercial pure aluminum or the modified alloy could result in a comparable performance, with an obvious cost reduction for the battery on the material supply.

However, limited research has been reported regarding the effects of Ca addition on the corrosion and discharge performance of aluminum alloy as anode for aluminum-air battery. In this paper, the commercial pure aluminum alloy 1070 with calcium addition is proposed as aluminum anodes of aluminum-air battery. By comparing the corrosion behaviors of aluminum anodes with different calcium contents, the aim of this study is to investigate the effects of calcium addition and the correlative intermetallic phase on the performance of the aluminum-air battery. Microstructure, corrosion rate, open-circuit potential (OCP), potentiodynamic polarization and electrochemical impedance spectroscopy (EIS) were implemented in the half cell assembly to analyse the performance of anodic dissolution. The constant current discharge in the full cell was studied to evaluate the performance of the aluminum-air battery.

2. EXPERIMENTAL PROCEDURES

2.1. Electrodes and electrolyte

The aluminum alloys were prepared by the stir cast method. The commercial pure aluminum 1070 was taken as the master alloy, which was melted and heated to a super-heated temperature of approximately 780 °C in a graphite crucible in an electric resistance furnace. Then, 99.99 wt.% pure calcium was added to the molten metal. When calcium was dissolved completely, the melt was stirred

well by a mechanical stirrer at a certain rpm to ensure complete homogenization of the alloying elements. The melt was isothermally held for several minutes before stirring stopped and then poured into a metallic mould preheated to 300 °C. The master aluminum alloy 1070 and pure calcium were provided by Sichuan Jinyue New materials Co., LTD, China, and Shanghai Shunyou Metallic Materials Co., China, respectively. The casting alloys were subjected to heat treatments in the following steps: a solution heat treatment (540 °C / 4 h) in an electrical oven, then quenching to cold water, followed by ageing at 140 °C for 2.5 h. The detailed compositions of the casting samples are listed in Table 1. The sample without calcium and those containing 0.075 wt.% Ca, 0.270 wt.% Ca and 1.140 wt.% Ca are denoted as 1#, 2#, 3# and 4# alloy, respectively. The 1# sample was obtained by recasting the master aluminum alloy. Metallography was used to observe the surface morphology of the specimens, and X-ray diffraction (XRD) was employed to determine the structural and phase information of the samples.

Table 1. Chemical compositions (wt.%) of aluminum anodes.

Sample	Component				
	Fe	Si	Zn	Ca	Al
1#	0.127	0.042	0.008	<0.001	Rem.
2#	0.218	0.171	0.029	0.075	Rem.
3#	0.229	0.270	0.035	0.270	Rem.
4#	0.228	0.334	0.035	1.140	Rem.

For electrochemical tests, specimens were small cubes (10 mm×10 mm×5 mm) cut from the above casting samples. All specimens were mounted in a soft mode and sealed with epoxy resin. The geometric surface area of each working electrodes was 1.0 cm², and they were mechanically ground and polished through standard routines. In addition, the specimens were ultrasonically cleaned in deionized water, rinsed in ethanol and dried with air.

The air cathode was rolled up by a Ni metal mesh, a catalytic layer consisting of MnO₂/C and PTFE and a waterproof layer consisting of PTFE, carbon materials and NaSO₄[7,21,22]. The electrolyte is 4 M KOH solution, as it possesses the peak electrolytic conductivity.

2.2. Full-cell assembly

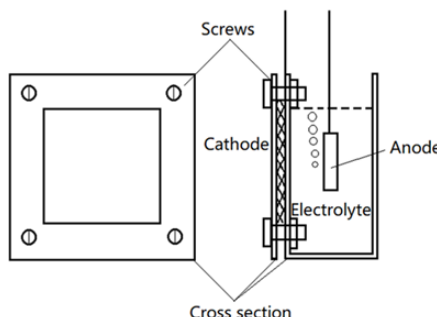


Figure 1. The schematic diagram of the assembled aluminum-air battery.

The full cell assembly for this study is shown in Fig. 1. This full cell was made up of the sample anode, the air cathode and an acrylic board. To prevent the limiting factors to the anode performance, the total reaction area of the cathode (25 cm^2) was oversized compared to the reaction area of the Al anode (1.0 cm^2).

2.3. Corrosion test

To further determine the corrosion rate, specimens were immersed in 4 M KOH for one hour. Before and after immersion, the weight of the specimens was measured and recorded. The rate of corrosion was defined as follows [23,24]:

$$\text{Corrosion rate (mm a}^{-1}\text{)} = 87.6 \frac{W}{DAt} \quad (2)$$

where W is the loss weight after the corrosion test (mg), D is the aluminum alloy density (g cm^{-3}), A is the reaction surface area (cm^2), and t is the self-corrosion test time (s).

2.4. Electrochemical measurements

The electrochemical performance evaluation in a three-electrode cell system was carried out with a GAMRY Reference 600+ electrochemical workstation under computer control. The electrolyte for those tests was 4 M KOH and the exposed area of anode was controlled at 1.0 cm^2 . The open circuit potential (E_{ocp}) test with a test time of 7200 s was carried out to evaluate the stability of reaction. The anodic oxidation reaction performance was investigated by the anodic polarization test. The anodic polarization curves were recorded at a scan rate of 1 mV s^{-1} . Electrochemical impedance spectroscopy (EIS) was carried out to evaluate the electrochemical behavior. This test was performed after a two-hour open circuit potential test and applied a sinusoidal wave. The frequency range of wave was from 10^5 to 10^2 Hz , and the amplitude of the wave was 5 mV. By using GAMRY Reference 600+ software, the equivalent circuit and parameters were obtained by fitting the experimental data.

2.5. Constant current discharge and characterization

The constant current discharge test was carried out by a GAMRY Reference 600+ electrochemical workstation under different current densities. Before and after the constant current discharge test, the cleaned anodes were both weighed and recorded. The efficiency and capacity density of the anode were defined as follows [18]:

$$\text{Efficiency (\%)} = \frac{Q_{\text{real}}}{Q} = \frac{100It}{\Delta mF/9} \quad (3)$$

$$\text{Capacity density (Ah g}^{-1}\text{)} = \frac{It}{3600\Delta m} \quad (4)$$

where Efficiency is the anode discharge efficiency (%), Q_{real} is the charge capacity of real external circuit, Q is the total charge capacity during discharge test, I is current through the external circuit during test (A), Δm is the loss weight after test (g), F is faraday constant and t is the discharge time (s).

All the above tests were repeated at least three times at room temperature.

Scanning electron microscopy (SEM) and energy dispersive X-ray spectroscopy (EDS) were used to investigate the surface morphology and corresponding element distributions of the specimens without surface cleaning after 1 h discharge in 4 M KOH.

3. RESULTS AND DISCUSSION

3.1. Corrosion behavior of the anodes

It is known that Al-air battery exhibits superior performance in alkaline electrolyte compared to other media. However, the polarization and corrosion of anodes in alkaline conditions are more serious, which influences the performance of the full battery. So, this section discusses the corrosion behavior of the calcium aluminum alloys in 4 M KOH.

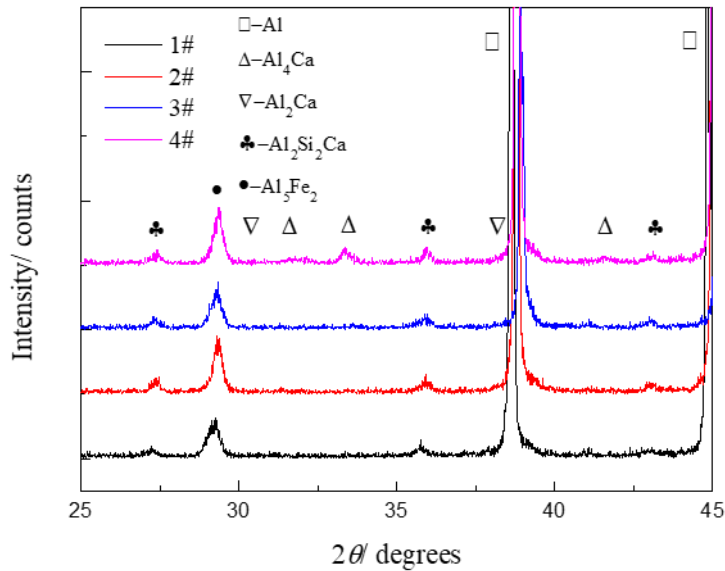


Figure 2. XRD pattern of the examined samples of 1070 aluminum alloy with different calcium addition contents.

The chemical compositions of the four examined anode samples are listed in table 1, and their XRD patterns are presented in Fig. 2. All the samples contain microelements of iron and silicon as impurities and form Fe-rich intermetallic phases. It is known that when the iron content exceeds its solid solubility (0.05 wt.%), the Fe-rich intermetallic phases (Al-Fe, Al-Fe-Si type) usually form in the aluminum alloy [25]. When Ca was added up to 0.270 wt.%, Ca-rich intermetallic phases (Al₄Ca and Al₂Ca) were observed as shown in Fig. 2. The metallographic graphs in Fig. 3 clearly show that Ca addition plays a significant role in refining the grain structure. First, as the calcium content increases, the dendrite structure and grain size become finer. Second, the morphology of the precipitates changed

significantly. As shown in Fig. 3(a), Fe-rich intermetallic phases, which are relatively coarse and unevenly distributed in the inter-dendritic region and grain boundaries in sample 1# sample without Ca addition. However, in sample 2# with trace of Ca addition, Fig. 3(b) shows the intermetallic phases are obviously uniform and fine, and a few extra particles within the arms of the dendrite or in the matrix. This signifies that the trace addition of Ca suppresses the formation of the eutectic phase and clearly decorates the alloy microstructure. As reported by others, trace impurity elements would form precipitates in aluminum alloys. When the alloy containing 39 ppm Ca and enough silicon, CaAl_2Si_2 might precipitate in A356 alloy or other aluminum alloys [26-28], and intermetallic precipitates of Al_4Ca and Al_2Ca will be formed when more Ca is added [29]. In this study, Fig. 2 shows that Ca-rich phases (Al_4Ca and Al_2Ca) are formed when the Ca content exceed 0.270 wt.%. The metallographic graph in Fig. 3(c) shows that more Ca-rich intermetallic precipitates are formed in sample 3# both along the inter-dendritic region and grain boundary with much bigger sizes. There are some larger particles look like the eutectic lamellar structure in blocks, which is consistent with the report that large particles are inhomogeneously distributed along the inter-dendritic region and grain boundaries in aluminum alloys containing calcium [29,30]. There are also some dispersed particles present within the arms or in the matrix. And Fig. 3(d) shows that the grain size become finer. When Ca was added up to 1.140 wt.%, as shown in Fig. 3(d), more lamellar structure blocks formed along the inter-dendritic region, grain boundary and even in the matrix.

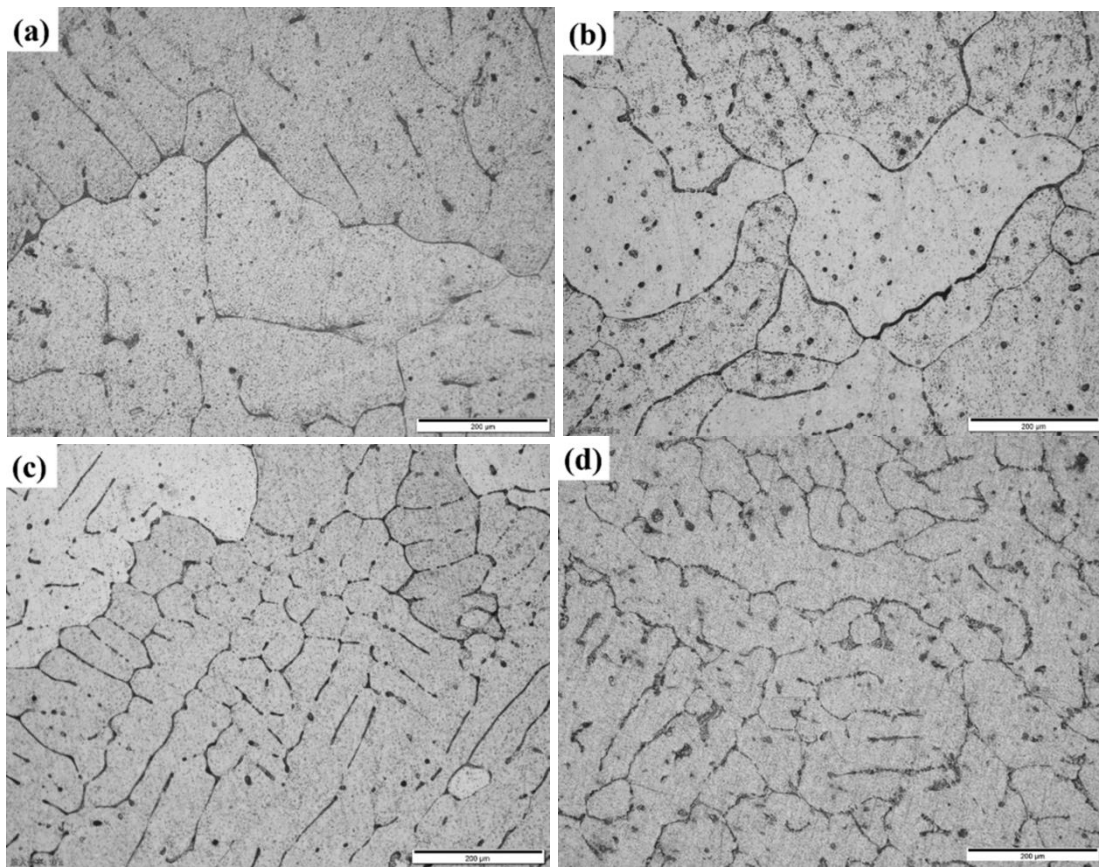


Figure 3. Metallography of examined samples corroded by 4 M KOH (a) 1# (b) 2# (c) 3# and (d) 4#.

The corrosion rate in 4 M KOH during discharge is a significant factor affecting the utilization efficiency of the anode for the Al-air battery. Table 2 gives the corrosion rate of the four anodes after one-hour immersion in 4 M KOH solution. It displays that corrosion rate decreases with increasing calcium addition. The sample 2# shows the fastest corrosion rate and sample 4# shows the lowest corrosion rate, which might due to distribution and the amount of Fe-Si-type impurities and the formation of the lamellar structure eutectic phases.

Table 2. Corrosion rate of aluminum anodes from the one-hour corrosion test in 4 M KOH.

Sample	Loss weight / mg	Corrosion rate / mm a ⁻¹
1#	40.7	1320
2#	80.3	2610
3#	41.0	1330
4#	35.4	1150

Fig. 4 shows the open circuit potentials (OCPs) of four anodes, and the values changed variously with the time elapsed. All anodes are polarized as soon as they are exposed to 4 M KOH solution, and all deteriorate over time. The open circuit potentials of sample 2# and 4# continuously shift to the maximum and minimum positive values at the end of 3000 s, respectively. The change in the voltage was less than 0.1 mV s⁻¹. An equilibrium was considered to be established, and the polarization of the four anodes was almost steady. After 5 hours, the steady open circuit potentials for the sample 1#, 2#, 3# and 4# anode reached -1.35 V, -1.33 V, -1.37 V, -1.39 V, respectively. These results demonstrate that the electrochemical activities of sample 3# and 4# are better than that of sample 1#. As shown in Fig. 3, sample 3# and 4# had more grain boundaries, which had more crystal defects and higher energy, and there were more channels for action, which were introduced by more grain boundaries, and these characteristics can improve their chemical activity [10].

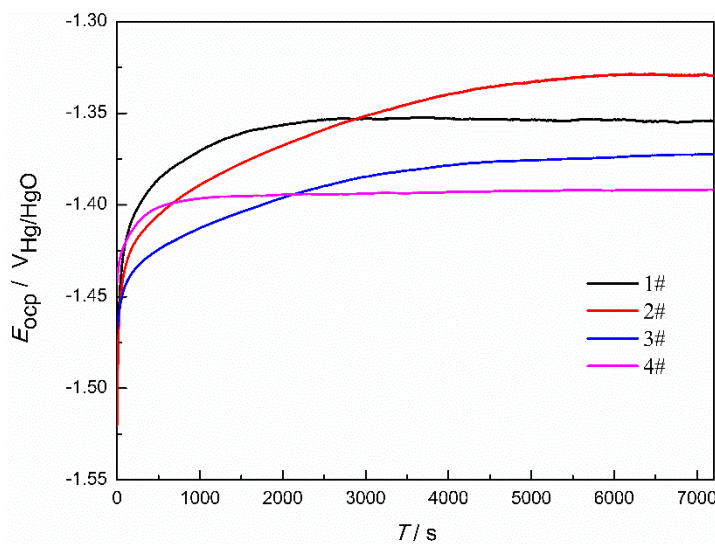


Figure 4. The change in the open circuit potentials with time (7200 s) for different anodes in 4 M KOH.

In this study, polarization curves and fitting result of sample 1#, 2#, 3# and 4# are shown in Fig. 5 and Table 3, which can be used to reflect the corrosion rate. The different cathodic Tafel slope (β_c) values of the four anodes indicate diverse cathodic kinetics, which should be linked to their different hydrogen evolution behavior. The anodic Tafel slope (β_a) of sample 4# is the minimum, which indicates that its discharge activity is strongest during anodic polarization [31]. In addition, although sample 2# and 4# display the most positive and negative corrosion potentials (E_{corr}), respectively, they show the highest and lowest corrosion current (I_{corr}), respectively, which indicates that the corrosion rate of sample 4# is minimized. The corrosion rates are as follows: 2# > 1# > 3# > 4#. The results are in good agreement with the corrosion test.

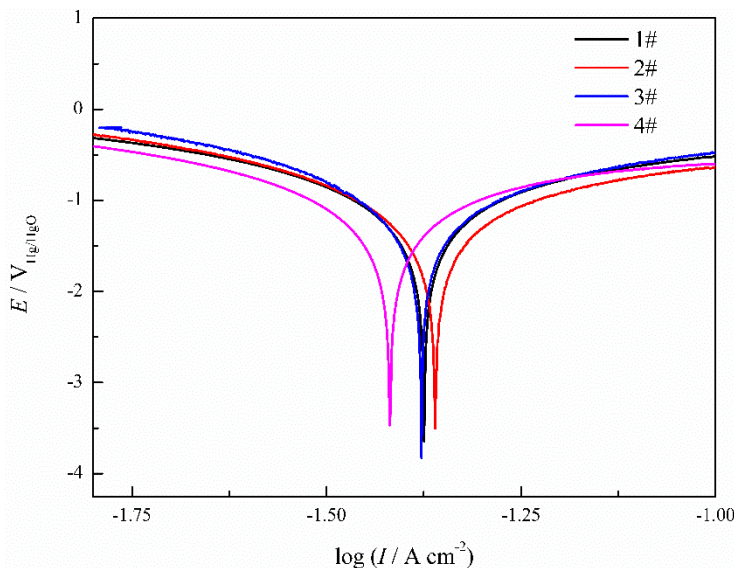


Figure 5. Anodic and cathodic polarization curves of four anodes for the half-cell in 4 M KOH.

Table 3. Electrochemical corrosion parameters of different anodes.

Sample	$\beta_A / \text{V dec}^{-1}$	$\beta_C / \text{V dec}^{-1}$	$E_{corr} / \text{V vs Hg/HgO}$	$I_{corr} / \text{mA cm}^{-2}$	Corrosion rate / mpy
1#	1.09	0.71	-1.37	199.0	85100
2#	3.03	0.74	-1.36	226.0	97100
3#	0.86	0.44	-1.38	141.0	60300
4#	0.49	0.40	-1.42	88.9	38100

The impedance spectra consisting of Nyquist and Bode curves are shown in Fig. 6. In general, the resistances in the EIS test include the solution resistance, R_s , and polarization resistance, R_p [32]. Polarization resistance contains the film resistance, R_{film} , and pore resistance, R_{por} , related to aluminum dissolution [18,24]. The figure in Fig. 6(a) shows that the four samples almost have the same shape with two loops, which is similar to the report of an aluminum alloy in alkaline by Mutluis [18]. One loop at high frequencies related to pore resistance (R_{por}), which includes the charge transfer resistance, R_{ct} , diffuse layer resistance, R_d , and other corrosion products accumulated (due to alloying elements, any existing molecules or ions), R_a , as well as another loop at low frequencies due to the film growth (R_{film}),

which includes $\text{Al(OH)}_3/\text{Al(OH)}^{4-}$ solution equilibrium on the anode surface and other surface protective layers formed by the alloying element Ca [33,34].

The electrical equivalent circuit diagram is presented in Fig. 7 to simulate the metal/solution interface, and the fitting impedance parameters are listed in Table 4. Here the constant phase element, *CPE*, replaces the capacitor to describe the inhomogeneous level of electrode surface. Due to the different reaction processes of four samples when they contact with the electrolyte, the conductivity of the electrolyte increases for electrode containing more calcium addition. This indicates that a certain amount of Ca^{2+} ions inhibit the production of hydrogen due to their strong affinity to OH^- [35]. More Ca(OH)_2 are produced for electrode with more Ca content. In addition, the impurity elements Fe and Si are redistributed and the lamellar structure eutectic phases are formed. Those all lead to the change in film resistance. The R_{por} of sample 3# and 4# continuously increase, and their values are 0.31 and $0.38 \Omega \text{ cm}^2$, respectively. However, the R_{por} of sample 2# sharply drops to $0.27 \Omega \text{ cm}^2$ which is even lower than that of sample 1#. Those might be related to their different anode dissolution for their different precipitated phases. Due to the influence of various factors, the polarization resistance values of sample 1#, 3# and 4# also show a rapid increase from $0.39 \Omega \text{ cm}^2$ to $0.41 \Omega \text{ cm}^2$, however, the polarization resistance value of sample 2# sharply drops to $0.33 \Omega \text{ cm}^2$, which is even lower than that of sample 1#. This result is in good agreement with the results of the above tests. It clearly shows that when the calcium content exceeds 0.270 wt.%, higher film or local pore resistance formed limits the corrosion process. Therefore, the polarization resistance of sample 4# has the maximum value. This result proves that the addition of 1.140 wt.% Ca decreases the corrosion of the aluminum anode.

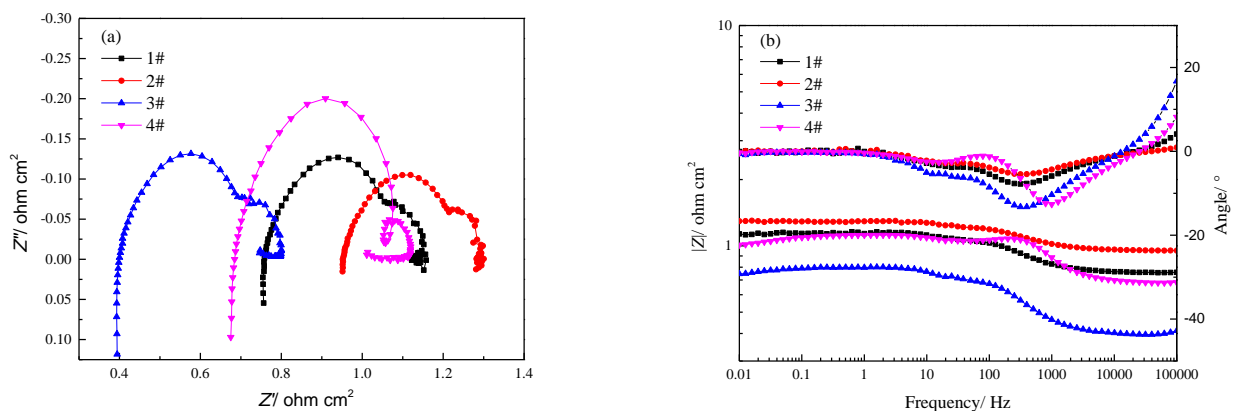


Figure 6. EIS measurements (7200 s) of four anodes in 4 M KOH (a) Nyquist and (b) Bode curves.

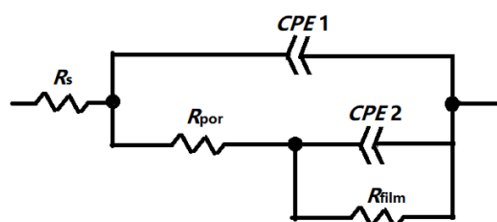


Figure 7. The equivalent circuit of different anodes for fitting the EIS plots.

Table 4. Fitting results of different anodes for the EIS plots from Figure 6.

Sample	R_s ($\Omega \text{ cm}^2$)	CPE_1	R_{por} ($\Omega \text{ cm}^2$)	CPE_2	R_{film} ($\Omega \text{ cm}^2$)	$R_p = R_{\text{por}} + R_{\text{film}}$ ($\Omega \text{ cm}^2$)		
1#	0.76	5.04E-3	0.85	0.32	0.14	1.00	6.52E-2	0.39
2#	0.95	6.10E-3	0.83	0.27	0.14	1.00	6.34E-2	0.33
3#	0.04	3.49E-3	0.90	0.31	0.12	1.00	8.08E-2	0.39
4#	0.07	4.36E-4	1.00	0.38	0.49	1.00	2.57E-2	0.41

3.2. Galvanostatic discharge test

The anodic behavior of the half-battery cell was tested by the galvanostatic discharge test of the anodes at the current densities of 1.00, 5.00, 10.00 and 30.00 mA cm^{-2} , as shown in Fig. 8. The findings demonstrate that the average discharge voltage of sample 2# is the highest, and the average discharge voltage of sample 4# is the lowest which is even lower than that of sample 1#. These phenomena can be explained by the different microstructures and chemical activation of the anodes shown above [18,36]. Therefore, the aluminum anode with 1.14 wt.% Ca shows the most negative voltage under different current densities.

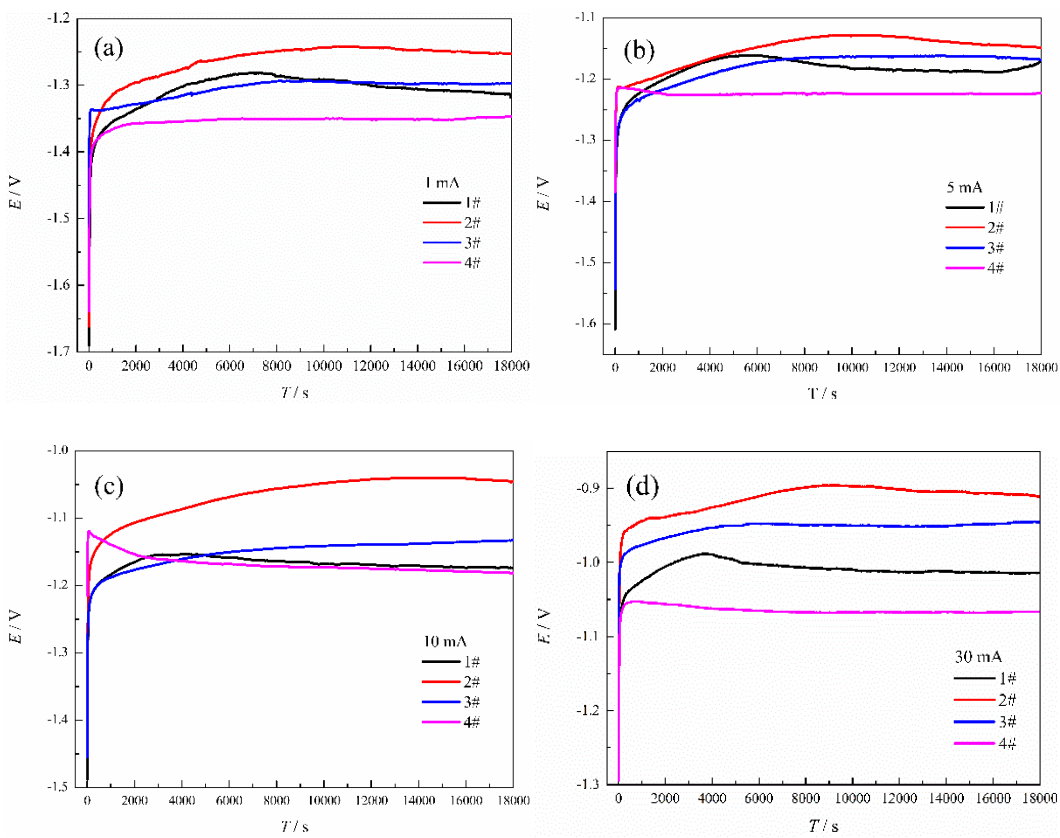


Figure 8. Discharge behavior of anodes (18000s) at different discharge currents: (a) 1 mA, (b) 5 mA, (c) 10 mA, (d) 30 mA.

Based on the galvanostatic discharge test, Table 5 displays the anode efficiencies and the capacity densities calculated according to equations (4) and (5). The anode efficiency and capacity density are related to the mass loss and discharge current density. Under the same discharge current density, the lower corrosion mass which inhibits the corrosion reaction, represents superior performance in terms of efficiency and the capacity density. In addition, the anode efficiency and the capacity density increased distinctly with the increase in the discharge current. This was caused by significantly increasing the proportion of the same anode corrosion for charge transfer, as shown in Table 4, and it is close to that of the aluminium-air batteries employed materials of Al-6013-T6 and Al-7075-T7351 as anodes [18].

Table 5. Galvanostatic discharge performance parameters of different anodes at different current densities.

Sample	$\Delta m / \text{mg}$	Current density / mA cm ⁻²	Efficiency / %	Capacity density / Ah g ⁻¹
1#	105.3	1.00	1.59	0.047
2#	167.7	1.00	1.00	0.030
3#	116.6	1.00	1.44	0.043
4#	85.6	1.00	1.96	0.058
1#	133.4	5.00	6.29	0.19
2#	160.3	5.00	5.24	0.16
3#	131.1	5.00	6.40	0.19
4#	118.3	5.00	7.09	0.21
1#	133.6	10.00	12.56	0.37
2#	170.2	10.00	9.87	0.29
3#	144.3	10.00	11.63	0.35
4#	134.0	10.00	12.53	0.37
1#	214.0	30.00	23.54	0.70
2#	266.4	30.00	18.91	0.56
3#	251.0	30.00	20.07	0.60
4#	232.3	30.00	21.68	0.65

At low discharge current (current density less than 5 mA), the anode efficiencies and capacity densities of the sample 4# electrode are higher than those of sample 1#, 2# and 3#, which means that the corrosion reaction was inhibited in sample 4#. Thus, the 4# anode is the best one. When the discharge current density increase to 10 mA, the 1# and 4# electrodes showed much better values. It is believed that the change in anode efficiencies and capacity densities is due to the polarization behavior of the anode and cathode under different discharge current density [36]. Overall, it is evident that calcium addition obviously affects the battery performance during charging.

The surface morphologies of different anodes charging in 4M KOH solution obtained by scanning electron microscopy are shown in Fig. 9 and Fig. 10. There are some distinct features of the charging surfaces. First, the degree of surface coverage of the four electrodes is markedly different, as

shown in Fig. 9. The impurity layer or discharging product is formed and becomes thicker and denser during discharge by dissolving the impurities on the electrode surfaces [37]. From the SEM images in Fig. 9, the surface coverage of sample 2# is much lower than samples 1# and 3#, and sample 4# has the highest coverage. Second, the morphologies of discharging products after charging for 60 min are different, as shown in Fig. 9. In the case of sample 1#, some smaller inclusions containing Fe and Si can be detected, as shown in Fig. 3a. As shown in Fig. 9a and Fig. 10a, the flocculate-like products occupy the surface. The corresponding element distribution patterns in Fig. 10 indicate that this layer consists of impurities containing Fe, O and Si. Furthermore, Fe and O elemental distribution, as shown in Fig. 10a, clearly indicate that the flocculent products are ferric oxide because their distribution patterns are completely coincident.

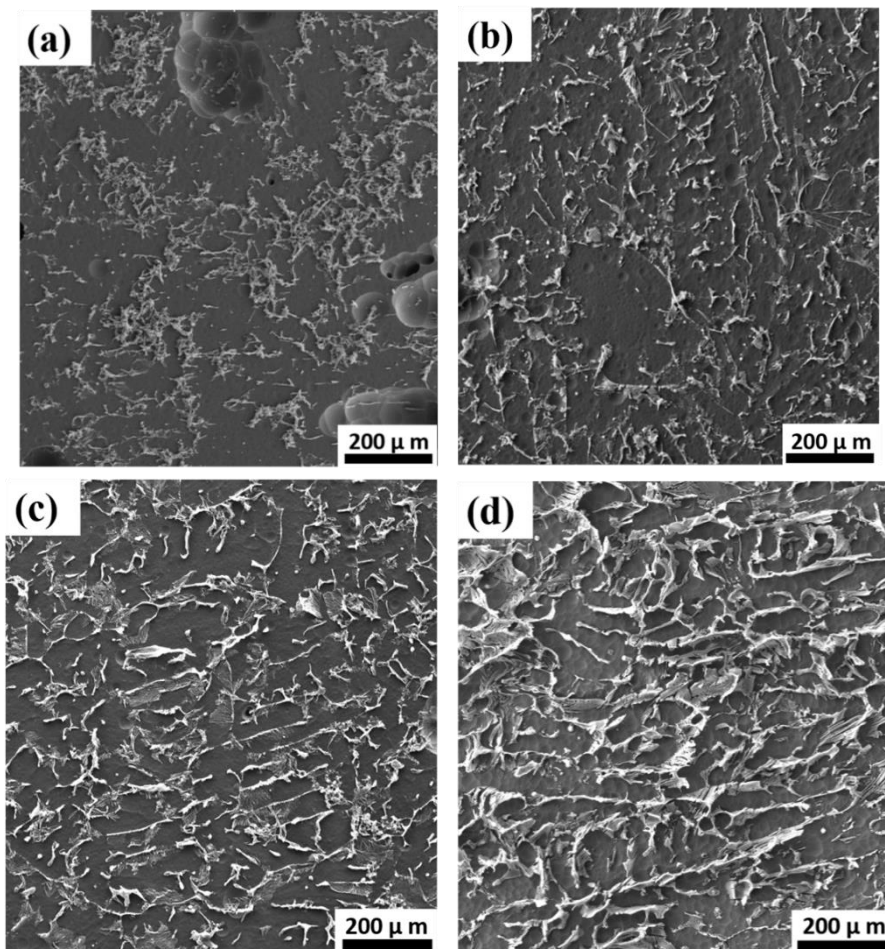


Figure 9. SEM (200 \times) measurements of the corrosion surface after 60 min of discharge at the low current density in 4 M KOH (a) 1#, (b) 2#, (c) 3# and (d) 4#.

There are some particles containing Fe and O, and some oxidation products of Fe segregate at the inter-dendritic region and grain boundaries in the form of inclusions. In sample 2#, as shown in Fig. 9b, except for the fewer flocculent products of iron oxides on the surface, some pieces of Fe-rich and Ca-rich inclusions can be observed along the inter-dendritic region and grain boundaries, some of them in lamellar structure as blocks formed via the eutectic reaction during heat treatment which is consistent with the Fig. 3b. For 0.270 wt.% Ca in sample 3#, as shown in Fig. 9c, flocculent products of iron oxides

occupy the surface and more Ca-rich phases formed. For 1.140 wt.% Ca, the surface morphology of sample 4#, as shown in Fig. 9d, is distinctly different from others. The flocculent product of iron oxides almost entirely absent; instead, Fe-rich and Ca-rich phases occupy the surface, largely with the eutectic laminar appearance. The corresponding elemental distribution, as shown in Fig. 10d, indicates that the Fe-rich and Ca-rich phases are also oxidized during discharge.

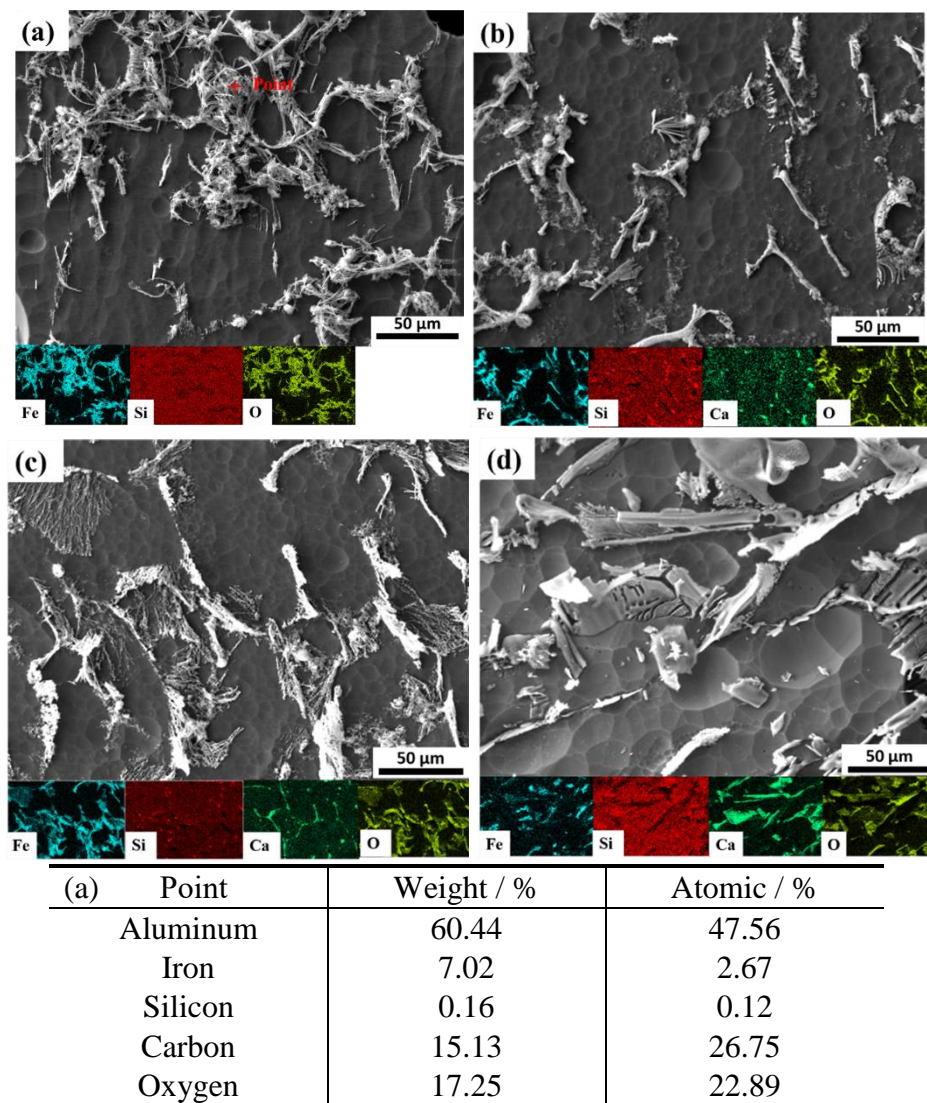


Figure 10. SEM (1000 \times) and EDS measurements of the corrosion surface after 60 min of discharge at low current density in 4 M KOH (a) 1#, (b) 2#, (c) 3# and (d) 4#.

As a function of Ca addition, the surface characteristics of the impurity layer on the discharging surface obviously depend on the Ca content; in turn, the impurity layer markedly affects the anode discharging behavior. First, the impurity element distribution and the characteristics of impurity oxides on the discharging surface are affected by Ca addition, or Ca addition markedly affects the characteristics of the impurity layer [29,38]. Without Ca addition, Fe as the main impurity element in sample 1# is extensively oxidized during discharging. The flocculent products of iron oxides may be related to the segregation of iron at the inter-dendritic region or grain boundaries. When Ca is added, more precipitates

are formed in the inter-dendritic region and grain boundaries. This means that the addition of Ca may reduce the solid solubility of the impurity elements Fe and Si in the aluminum alloy, which then segregate at the inter-dendritic region or grain boundaries to form inclusions [29,30,39]. Compared with sample 1#, Fe redistributed in other samples, and more Fe-rich and Ca-rich phases can be found. This changed the discharge products that occupied the surface and were obviously oxidized. For 1.140 wt.% Ca in sample 4#, the distribution of impurity elements was changed completely and more precipitates were observed. Thus, the discharge surface was occupied by Fe-rich and Ca-rich phases, which emerged as inclusions and were oxidized. These impurity inclusions and their oxides cover most of the surface and significantly reduce the corrosion rate and improve the performance of the Al-air battery.

4. CONCLUSIONS

The effects of Ca addition on the corrosion and discharge performance of commercial pure aluminum alloy 1070 used as the anode in aluminum-air battery were studied. Microstructure observations show that calcium addition significantly modifies the microstructure of the commercial pure aluminum. With increasing calcium content, the dendrite structure and grain size become finer, the impurity elements Fe and Si tend to segregate in the alloys, and more intermetallic phases are distributed along the inter-dendritic region, grain boundary and in the matrix as the product of the eutectic reaction.

Aluminum alloy anodes containing higher Ca content have higher polarization resistance and higher discharge voltage and also exhibit superior the better anode efficiency and capacity density. SEM observation shows that the impurity layer formed on the discharge surface can serve as a corrosion inhibitor and have positive effects on corrosion.

References

1. S. Zaromb, *J. Electrochem. Soc.*, 109 (1962) 1125.
2. S. Yang and H. Knickle, *J. Power Sources*, 112 (2002) 162.
3. Q. Li and N.J. Bjerrum, *J. Power Sources*, 110 (2002) 1.
4. M. Mokhtar, M.Z.M. Talib, E.H. Majlan, S.M. Tasirin, W.M.F.W. Ramli, W.R.W. Daud and J. Sahari, *J. Ind. Eng. Chem.*, 32 (2015) 1.
5. H.G. Schwarz, *Encyclopedia of Energy*, 1 (2004) 81.
6. M. Pino, J. Chacón, E. Fatás and P. Ocón, *J. Power Sources*, 299 (2015) 195.
7. Y. Liu, Q. Sun, W. Li, K.R. Adair, J. Li and X. Sun, *Green Energy & Environment*, 2 (2017) 246.
8. D.R. Egan, C.P.D. León, R.J.K. Wood, R.L. Jones, K.R. Stokes and F.C. Walsh, *J. Power Sources*, 236 (2013) 293.
9. M.A. Rahman, X. Wang and C. Wen, *J. Electrochem. Soc.*, 160 (2013) A1759.
10. L. Fan, H. Lu and J. Leng, *Electrochim. Acta*, 165 (2015) 22.
11. J. Ma, J. Wen, J. Gao and Q. Li, *J. Power Sources*, 253 (2014) 419.
12. I. Smoljko, S. Gudić, N. Kuzmanić and M. Kliskic', *J. Appl. Electrochem.*, 42 (2012) 969.
13. S.Z.E. Abedin and F. Endres, *J. Appl. Electrochem.*, 34 (2004) 1071.
14. D.D. Macdonald, S. Real and M. Urquidi-Macdonald, *J. Electrochem. Soc.*, 135 (1988) 2397.
15. M. Nestoridi, D. Pletcher, R.J.K. Wood, S. Wang, R.L. Jones, K.R. Stokes and I. Wilcock, *J. Power*

- Sources, 178 (2008) 445.
- 16. R. Liang, Y. Su, X.L. Sui, D.M. Gu, G.S. Huang and Z.B. Wang, *J. Solid State Electr.*, (2018).
 - 17. P. Montagné and M. Tillard, *J. Solid State Electr.*, 19 (2015) 685.
 - 18. R.N. Mutlu, S. Ateş and B. Yazıcı, *Int. J. Hydrogen Energ.*, 42 (2017) 23315.
 - 19. M. Pino, C. Cuadrado, J. Chacón, P. Rodríguez, E. Fatás and P. Ocón. *J. Appl. Electrochem.*, 44 (2014) 1371.
 - 20. J. Ma, J. Wen, J. Gao and Q. Li. *Electrochim. Acta.*, 129 (2014) 69.
 - 21. J.S. Lee, G.S. Park, H.I. Lee, S.T. Kim, R. Cao, M. Liu and J. Cho, *Nano Letters*, 11 (2011) 5362.
 - 22. L. Mao, D. Zhang, T. Sotomura, K. Nakatsu, N. Koshiba and T. Ohsaka, *Electrochim. Acta*, 48 (2003) 1015.
 - 23. D.A. Jones, Principles and prevention of corrosion, *Prentice Hall*, (1996) NJ, USA.
 - 24. Y.J. Cho, I.J. Park, H.J. Lee and J.G. Kim, *J. Power Sources*, 277 (2015) 370.
 - 25. P. Skjerpe, *Metall. Mater. Trans. A*, 18 (1987) 189.
 - 26. T.H. Ludwig, E.S. Dæhlen, P.L. Schaffer and L. Arnberg, *J. Alloy. Compd.*, 586 (2014) 180.
 - 27. S. Wenner, C.D. Marioara, S.J. Andersen and R. Holmestad, *Mat. Sci. Eng. A*, 575 (2013) 241.
 - 28. T.H. Ludwig, P.L. Schaffer and L. Arnberg, *Metall. Mater. Trans. A*, 44 (2013) 3783.
 - 29. D.P. Mondal, N. Jha, A. Badkul, S. Das, M.S. Yadav and P. Jain, *Mater. Design*, 32 (2011) 2803.
 - 30. Q. Lu, Y. Shen, S. Zhong, C. Zhao and W. Long, *Rare Metal Mat. Eng.*, 47 (2018) 1739.
 - 31. H. Xiong, K. Yu, X. Yin, Y. Dai, Y. Yan and H. Zhu, *J. Alloy. Compd.*, 708 (2017) 652.
 - 32. I.J. Park, S.R. Choi and J.G. Kim, *J. Power Sources*, 357 (2017) 47.
 - 33. K.C. Emregül and A.A. Aksüt, *Corros. Sci.*, 42 (2000) 2051.
 - 34. R. Solmaz, *Corros. Sci.*, 52 (2010) 3321.
 - 35. Z. Zhao, X. Chen and M. Hao, *Energy*, 36 (2011) 2782.
 - 36. L. Fan and H. Lu, *J. Power Sources*, 284 (2015) 409.
 - 37. J. Wang, J. Wang, H. Shao, J. Zhang and C. Cao, *J. Appl. Electrochem.*, 37 (2007) 753.
 - 38. M. Deng, D. Höche, S.V. Lamaka, D. Snihirova and M.L. Zheludkevich, *J. Power Sources*, 396 (2018) 109.
 - 39. S.S. Sreeja Kumari, R.M. Pillai and B.C. Pai, *Int. Mater. Rev.*, 50 (2005) 216.